Possible Hundredfold Enhancement in the Direct Magnetic Coupling of a Single-Atom Electron Spin to a Circuit Resonator

Bahman Sarabi,[1,2,*] Peihao Huang,[1,2] and Neil M. Zimmerman[1]

[1]*National Institute of Standards and Technology, Gaithersburg, Maryland 20899, USA*
[2]*Joint Quantum Institute, University of Maryland, College Park, Maryland 20742, USA*

We report on the challenges and limitations of direct coupling of the magnetic field from a circuit resonator to an electron spin bound to a donor potential. We propose a device consisting of a trilayer lumped-element superconducting resonator and a single donor implanted in enriched ^{28}Si. The resonator impedance is significantly smaller than the practically achievable limit obtained with prevalent coplanar resonators. Furthermore, the resonator includes a nanoscale spiral inductor to spatially focus the magnetic field from the photons at the location of the implanted donor. The design promises an increase of approximately 2 orders of magnitude in the local magnetic field, and thus the spin-to-photon coupling rate g, compared with the estimated rate of coupling to the magnetic field of coplanar transmission line resonators. We show that by use of niobium (aluminum) as the resonator's superconductor and a single phosphorous (bismuth) atom as the donor, a coupling rate of $g/2\pi = 0.24$ MHz (0.39 MHz) can be achieved in the single-photon regime. For this hybrid cavity-quantum-electrodynamic system, such enhancement in g is sufficient to enter the strong-coupling regime.

I. INTRODUCTION

Silicon-based spin qubits, including gate-defined quantum dot [1–3] and single-atom [4,5] devices, use the spin degree of freedom to store and process quantum information, and are promising candidates for future quantum electronic circuits. The electronic or nuclear spin is well decoupled from the noisy environment, resulting in extremely long coherence times [6–8], which are desirable for fault-tolerant quantum computing. Single-atom electron spin qubits offer additional advantages over quantum dot qubits, such as longer coherence due to strong confinement potentials, and are expected to have intrinsically better reproducibility. Therefore, it is no surprise that silicon-based single-atom electron spin qubits hold the record coherence times of any solid-state single qubit [9]. However, this attractive isolation from sources of decoherence comes at the price of relatively poor coupling to the control and readout units. This causes relatively long qubit initialization times, degraded readout fidelity, and weak spin-spin coupling for multiqubit operations [10].

One simple way to enhance the coupling rate is to increase the ac magnetic field from the external circuit. In this regard, superconducting circuit resonators are attractive due to their relatively large quality factors, ease of coupling to other circuits, their capability of

generating relatively large ac magnetic fields by carrying relatively large currents, and monolithic integration with semiconductor devices.

Over the last two decades, superconducting microwave resonators have had extensive applications that range from superconducting-qubit initialization, manipulation, and readout [11,12] and interqubit coupling [13] to dielectric characterization [14]. One of the most commonly used superconducting quantum computing architectures is one based on cavity quantum electrodynamics (cQED) [15], in which a two-dimensional (circuit-based) or three-dimensional cavity is used to initialize, manipulate, and readout the superconducting qubit. Superconducting circuit cavities have not yet found a similar prevalence in spin-qubit circuits because the magnetic field of a typical superconducting resonator and the spin magnetic-dipole moment are relatively small, leading to an insufficient spin-photon coupling strength for practical purposes. The direct magnetic coupling of coplanar resonators [typically coplanar waveguide (CPW) resonators] to donor electrons in silicon [16–18] and diamond nitrogen-vacancy centers [19,20] can achieve a maximum single-spin coupling rate of only a few kilohertz.

Several methods have been proposed to enhance the coupling of a single spin to a superconducting circuit resonator. It is easier to couple a photon to quantum dot spin qubits than to single-atom electron spins because in the former, the spin dynamics can be translated into an

_____
*bahman.sarabi@gmail.com

electric dipole interacting with the resonator's electric field [21–23]. Such architectures, however, require hybridization of the spin states with charge states, coupling charge noise to the spin and thus affecting its coherence. For instance, in two recent experimental demonstrations of strong spin-photon coupling in Si [24,25], the maximum value of the figure-of-merit ratio of the coupling rate to the spin decoherence rate was about 5, due in part to the approximately-factor-of-5 increase in the dephasing rate [25] arising from the hybridization of spin and charge states. For the single-atom electron spin qubits, indirect coupling to a resonator via superconducting qubits [26,27] can enhance the coupling, but imposes nonlinearity on the circuit complicating cQED analysis, and also introduces loss from Josephson junction tunnel barriers [28,29] and magnetic flux noise [30].

In this paper, we show that replacing the coplanar-transmission line resonator with a lumped-element circuit resonator that includes a spiral inductor can lead to a dramatic enhancement in the spin-photon magnetic coupling rate g of approximately 2 orders of magnitude. As we discuss, this improvement is a result of the reduced resonator impedance thanks to the trilayer lumped-element design, as well as the use of nanoscale spiral inductor loops that effectively localize the resonator's magnetic field at the location of the spin, eliminating the need for an Oersted line [31] or a micrometer-scale magnet (micromagnet) [24,32]. We also show that this coupling rate is enough to take the spin-resonator hybrid system to the strong-coupling regime, where g is larger than or approximately equal to the resonator decay rate κ. To achieve this relatively large g, we need a relatively small total inductance L_{tot}, and concomitantly a small impedance $Z = \sqrt{L_{\text{tot}}/C}$. To reach the desired operation frequency $\omega_0 = \sqrt{1/L_{\text{tot}}C}$, we need a large capacitance C, and thus coplanar interdigitated capacitances are practically insufficient. Furthermore, interdigitated capacitances generally introduce relatively large parasitic inductance, which could set a limit to the minimum achievable Z. Therefore, the proposed device geometry, compatible with standard micro- and nanofabrication techniques, includes a trilayer (parallel-plate) capacitor with a deposited insulating layer. Trilayer capacitors, however, give rise to a lower resonator quality factor Q than that of a typical coplanar geometry. Nevertheless, as our calculations show, the increase in g resulting from use of a trilayer lumped-element design is large enough to overcome the limited Q, allowing strong spin-photon coupling.

II. SINGLE-ATOM DEVICE

The lossless dynamics of a spin-$\frac{1}{2}$ system with spin transition frequency ω_s coupled with rate g to a cavity resonant at ω_0 are described by the Jaynes-Cummings Hamiltonian: $\mathcal{H}_{\text{JC}} = \hbar\omega_0(\hat{a}^\dagger\hat{a} + 1/2) + (1/2)\hbar\omega_s\hat{\sigma}^z + \hbar g(\hat{a}^\dagger\hat{\sigma}^- + \hat{\sigma}^+\hat{a})$

[33], where $\hat{a}$ and $\hat{\sigma}$ are photon and spin operators, respectively. The spin-photon magnetic coupling rate is obtained as $g = g_e\mu_B B_{\text{ac},0}\langle g|\hat{S}_x|e\rangle/\hbar$, where $g_e \simeq 2$ is the electron g-factor, μ_B is the Bohr magneton, and $B_{\text{ac},0} = \langle n = 0|\hat{B}_{\text{ac}}^2|n = 0\rangle^{1/2}$ is the root-mean-square (rms) local magnetic field at the location of the spin with $n = 0$ photons on resonance. $|g\rangle$ and $|e\rangle$ are the ground-state and excited spin state, respectively, that couple to the microwave field; for spin $\frac{1}{2}$, $\langle g|\hat{S}_x|e\rangle = 1/2$. Finally, the spin rotation speed can be enhanced with a larger local rms magnetic field $B_{\text{ac}} = \langle n|\hat{B}_{\text{ac}}^2|n\rangle^{1/2}$ for any arbitrary n.

A schematic and the layout of the proposed circuit are shown in Fig. 1, where an LC resonator is coupled to a CPW by a direct (galvanic) connection through a coupling inductor L_c and the donor is within the resonator's deliberate (geometric) inductor L_g. The galvanic coupling, used in previous experiments [34], can help to achieve the desired CPW-resonator coupling rates especially when the resonator impedance is significantly different from the CPW's characteristic impedance $Z_0 = 50\ \Omega$. The capacitance C is provided with a trilayer capacitor. The rms current through the inductor at an average photon number $\bar{n}$ on resonance is $I_{\text{ac}} = \sqrt{(\bar{n} + 1/2)\hbar\omega_0/L_{\text{tot}}}$, where ω_0 is the resonance frequency and L_{tot} denotes the total inductance within the resonator circuit. Since the desired ac magnetic field from the spiral loop(s) is proportional to I_{ac}, it is clear that L_{tot} (or Z) must be minimized and the photon frequency must be maximized to obtain the maximum magnetic field. Therefore, it is necessary to study the sources of inductance and obtain operation-frequency limitations.

We study two sets of materials, one that uses niobium as a superconductor and phosphorous as a donor (Nb/P), and one with aluminum as a superconductor and bismuth as a donor (Al/Bi). Fabrication is considered to be slightly better established with Al, whereas Nb has a much higher critical magnetic field of $B_{c1,\text{Nb}} = 0.2$ T, which is the highest B_{c1} among the single-element superconductors. Through the Zeeman effect, for the Nb/P set, the uncoupled electron spin-up ($|\uparrow\rangle$) and spin-down ($|\downarrow\rangle$) states are split by the photon frequency $\omega_0/2\pi = 5.6$ GHz at the maximum $B_0 = \hbar\omega_0/g_e\mu_B \simeq B_{c1,\text{Nb}}$, not to quench superconductivity. For the Al/Bi set, we consider operating at $B_0 < 10$ mT (below the critical magnetic field of Al), and use the splitting of the spin multiplets ($\omega_0/2\pi = 7.375$ GHz) of the Bi donor. These splittings arise from the strong hyperfine interaction between the electron ($S = 1/2$) and Bi nuclear spin ($I = 9/2$) [35], leading to a total spin F and its projection m_F along $\mathbf{B_0}$. By use of the $|F, m_F\rangle = |5, -5\rangle \leftrightarrow |4, -4\rangle$ transition corresponding to the largest $\hat{S}_x$ matrix element (0.47) and a static magnetic field of $B_0 = 5$ mT, the multiplet degeneracy at $B_0 = 0$ is lifted by more than 20 MHz [36,37], enough to decouple the nearby transitions.
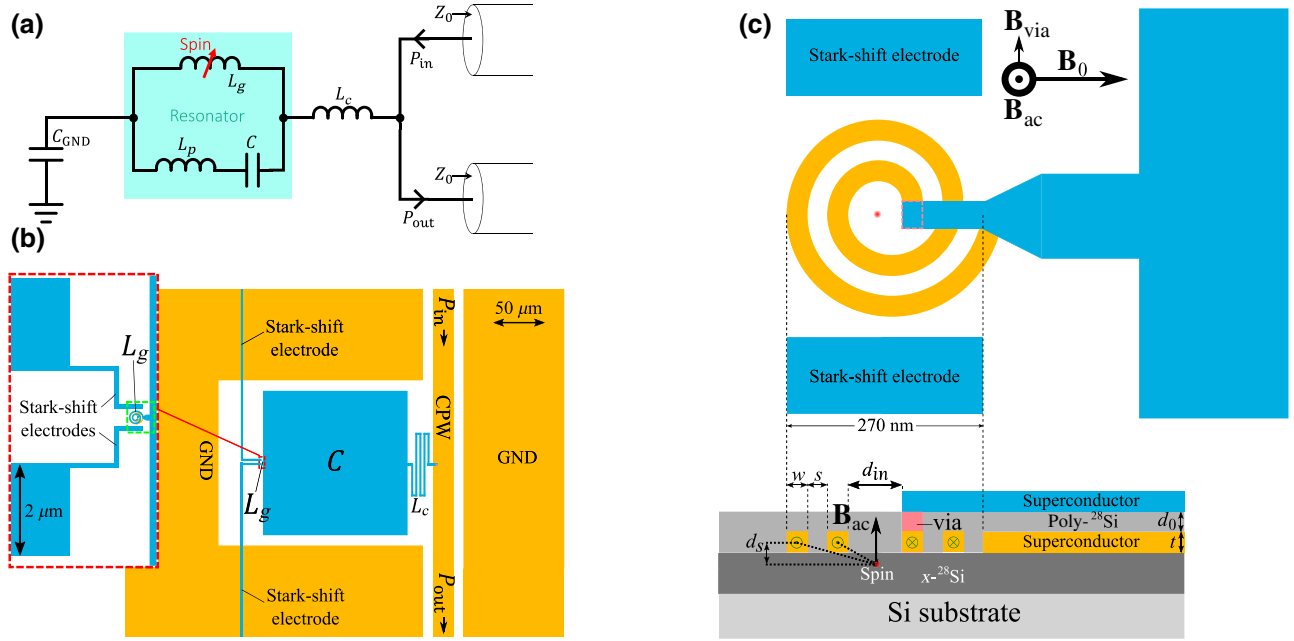
FIG. 1. (a) The circuit showing the resonator galvanically coupled to the CPW. C_{GND} is the resonator's capacitance to ground (GND). P_{in}, P_{out}, L_g, and L_p are the microwave input power, output power, geometric inductance, and parasitic inductance of the resonator circuit, respectively. (b) Layout of the device showing the resonator's capacitor C and inductor L_g. Blue and orange show the top and bottom superconducting layers, respectively. The area within the dashed red square is magnified. The spiral inductor within the dashed green square is further magnified to show (c) the single-spiral geometry (red dot represents the spin). The dimensions are $w = s = t = d_{in}/2 = 30$ nm, which are compatible with standard electron-beam lithography, and $d_0 = d_s = 25$ nm. The crystalline ^{28}Si (x-^{28}Si) growth is required only in the volume surrounding the spin, and amorphous or polycrystalline Si is acceptable everywhere else. The relatively weak magnetic field $\mathbf{B}_{via}$ from the via determines the best choice for the direction of the static magnetic field, $\mathbf{B}_0 \parallel (\mathbf{B}_{via} \times \mathbf{B}_{ac})$, where $\mathbf{B}_{ac}$ is the magnetic field from the spiral inductor (directions shown represent magnetic fields at the location of the spin). This ensures that the total ac field is perpendicular to $\mathbf{B}_0$. The current flowing through the spiral inductor is shown by green in-plane or out-of-plane vectors.

Figure 2 shows an alternative double-spiral (2S) geometry where the spiral inductor extends to both superconducting layers. Here we see the following optimum combination of materials: (i) Amorphous or polycrystalline Si can be deposited on the metal layers; since they have permittivities similar to the permittivity of crystalline Si, the capacitor size will be similar. (ii) Since the spin does not have a metal layer below it, one can still deposit crystalline ^{28}Si and then implant the donor, thus avoiding the fast decoherence that would otherwise result from the noncrystalline, nonenriched films [38]. From the fabrication point of view, it is easiest to use the same ^{28}Si film as the capacitor dielectric [see Figs. 1(c) and 2]. It is noteworthy that use of a trilayer design makes the resonator quality factor effectively independent of the surrounding material as almost all the electric field energy is confined within the capacitor dielectric. This is useful for the integration of single-electron devices that require lossy oxide layers.

For all four aforementioned combinations of resonator material and geometry, L_{tot} is simulated and shown in Fig. 3(a) as a function of the number of spiral loops, N_{loops} (see the Appendix for the details of inductance calculations and simulations). N_{loops} refers to the number of loops in a

single spiral layer regardless of the geometry; for example, $N_{loops} = 2$ for both Fig. 1(c) and Fig. 2. Increasing N_{loops} from 1 to 2 increases $B_{ac,0}$, but, for $N_{loops} > 2$, the competing effect of larger L_{tot} due to larger loop radii suppresses I_{ac} and lowers g. This effect is clearly demonstrated in Fig. 3(b) as the optimum $N_{loops} = 2$ for both material sets, where the vacuum fluctuations' coupling rates for the Al/Bi and Nb/P configurations are obtained as $g/2\pi = 0.26$ MHz and 0.17 MHz, respectively. For the 2S geometry, the coupling rates for the Al/Bi and Nb/P configurations approach $g/2\pi = 0.39$ MHz and 0.24 MHz, respectively. These values are approximately 2 orders of magnitude larger than for the previously proposed architectures that use coplanar transmission line resonators [18]. This new regime of g can enable new experiments such as individual-spin spectroscopy with direct magnetic coupling, and as we report in Sec. IV, it can lead to significant improvements in spin-qubit performance in regard to qubit initialization, manipulation, and readout.

Figure 3(c) shows the current density $J = (1/wt)I_{ac}|_{\bar{n}=0}$ of vacuum fluctuations for each configuration, where w and t are the width and thickness of the spiral traces, respectively [see Figs. 1(c) and 2]. Clearly, J stays far below the
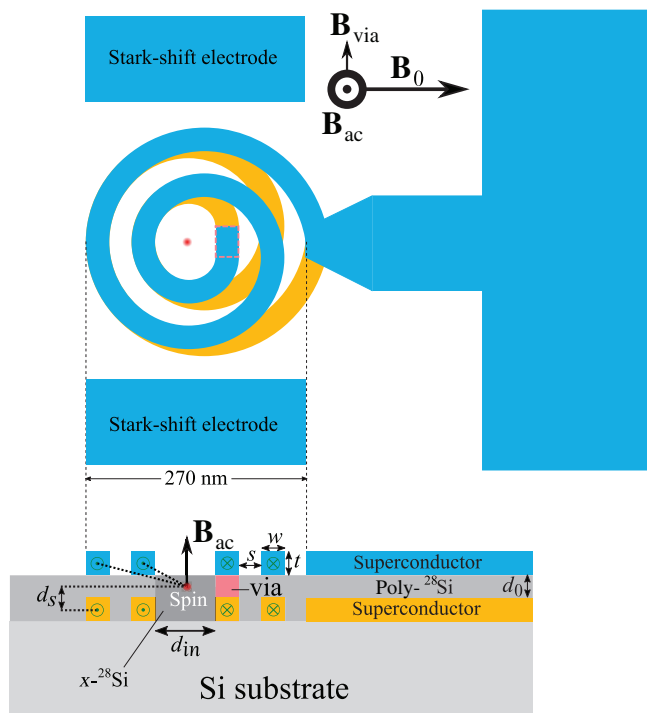
FIG. 2. Layout of the 2S device in the vicinity of the nanoscale spiral inductor. Here $d_s = 27.5$ nm, and other dimensions are identical to those in Fig. 1(c).

critical current values of Al ($J_c \sim 10^4$ kA/cm^2 [39]) and Nb ($J_c \sim 10^3$ kA/cm^2 [40]).

The condition for the system to enter the strong-coupling regime is $Q \gtrsim Q_0 \equiv \omega_0/g$ in the single-photon regime, where $Q = \omega_0/\kappa$ and κ are the resonator's total quality factor and total photon decay rate, respectively. Thanks to the relatively large spin-photon coupling rate, resonator quality factors on the order of 10^4 are enough to take the system to the strong-coupling regime for all four configurations [see Fig. 3(d)]. In general, in the limit of low drive power and low temperature, trilayer resonators are significantly lossier than coplanar resonators because almost all the photon electric energy is stored within the parallel-plate capacitor dielectric, which contains atomic-scale defects. These defects act as lossy two-level fluctu-ators at small powers and low temperatures, and limit the resonator Q [29]. However, loss tangents in the vicinity of $\tan \delta_0 \simeq 10^{-5}$ have been measured for deposited amor-phous hydrogenated silicon at single-photon energies [41], promising resonator Q values approaching 10^5. More recently, elastic measurements have indicated the absence of tunneling states in a hydrogen-free amorphous sili-con film, suggesting the possibility of depositing "perfect" silicon [42], promising even-higher-Q trilayer resonators with the use of silicon as the capacitor dielectric.

It was shown that the donor can be ionized in the vicinity of metallic or other conductive structures due to

energy-band bendings [38]. For an Al-Si interface, the relatively small work function difference of -30 meV (4.08 eV for Al and 4.05 eV for Si) is smaller than the donor-electron binding energy of -46 meV [43], and hence use of aluminum is expected to allow the donor bound state. However, the Nb work function of 4.3 eV causes significant band bending, which can result in donor ionization. By biasing the microwave transmission line and hence the resonator through the galvanic connection with a dc voltage, one can modulate the potential-energy land-scape in the neighborhood of the donor to recreate a bound state. If a conduction-band electron is required to fill the bound state, solutions such as shining a light pulse from a light-emitting diode to create excess electron-hole pairs or using an Ohmic path to controllably inject electrons can be used.

From Fig. 3(d) and the data available from silicon-based low-loss deposited dielectrics, we infer that the pro-posed single-atom device can achieve the strong-coupling regime. In general, the single-spiral design is expected to be easier to fabricate at the expense of a smaller g compared with the 2S geometry.

III. SIMPLIFIED DEVICE WITH SPIN ENSEMBLE

We now discuss a greatly simplified proof-of-principle device. We consider a low-impedance trilayer resonator on top of a Bi-doped substrate or ^{28}Si layer, and pro-pose measuring the spectrum in the single-photon regime while the electron spin transitions are tuned across the resonator bandwidth. Similarly to the single-atom device, tuning of the spins can be performed with magnetic (Zee-man) or electric (Stark, see Fig. 1) fields, or a combination of both. For further simplification, a single inductor loop with dimensions compatible with standard photolithogra-phy can be used. In this simplified experiment with *no single-donor-implantation or electron-beam-lithography requirements*, one can choose Al as a superconductor and thus the kinetic inductance within the circuit is negligi-ble with micrometer-scale dimensions of the inductor loop. When N_s spins are incorporated and exposed to the rela-tively uniform magnetic field inside the inductor loop, the collective coupling rate from the spin ensemble becomes $g_{\mathrm{col}} = g\sqrt{N_s}$ [17].

Since the spin-ensemble device is of micrometer scale, high-frequency simulations using electromagnetic simula-tion software are feasible (SONNET is used for this work). The layout of the simulated device is shown in Fig. 4(a). We use a galvanic connection to couple this device to the CPW, similar to the single-atom device described in Sec. II. As shown in Fig. 4(b), in the absence of donors, the simulated transmission $S_{21} = V_{\mathrm{out}}/V_{\mathrm{in}}$ through the CPW shows a characteristic resonance circle with a diameter of 0.5. This indicates that, because of the galvanic cou-pling and despite $Z \simeq 0.4 \ \Omega \ll Z_0$, critical coupling can
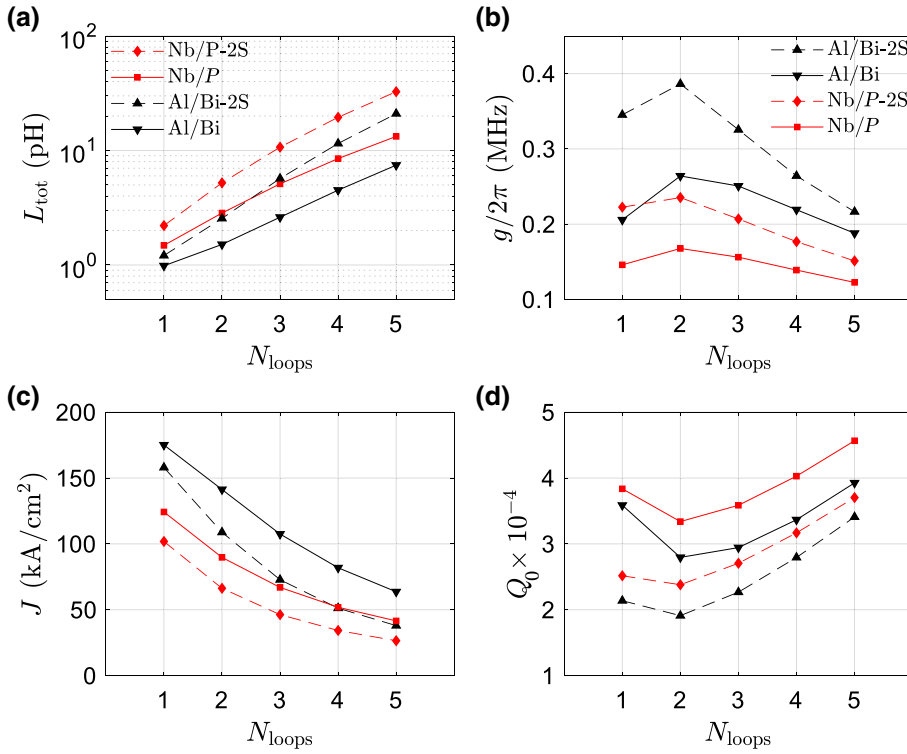
FIG. 3. (a) Total inductance, (b) spin-photon coupling rate, (c) current density of vacuum fluctuations, and (d) required resonator quality factor Q_0 to allow strong spin-photon coupling versus the number of spiral loops N_{loops} for different combinations of materials and geometries; that is, superconducting aluminum and bismuth donor (Al/Bi), superconducting niobium and phosphorous donor (Nb/P), single-spiral and 2S geometries.

be achieved, where the resonator external quality factor $Q_e \equiv \omega_0/\kappa_e$ equals its internal quality factor $Q_i \equiv \omega_0/\kappa_i$. Here κ_e is the resonator's photon loss rate through coupling to the CPW and κ_i is the resonator's decay rate due to its internal losses, and we have $\kappa = \kappa_e + \kappa_i$. In this simulation, we assume $\tan\delta_0 = 10^{-4}$ for the capacitor dielectric.

We adjust Q_e through simulation; we target $Q_e = Q_i$ to optimize the coupling while maintaining the resonator's coherence by avoiding a large κ_e. This critical CPW-resonator coupling regime cannot be practically achieved with typical capacitive-coupling geometries, and motivated the galvanic coupling scheme. We estimate that in this device the galvanic connection enhances κ_e by approximately 1 order of magnitude compared with capacitive coupling with dimensions compatible with standard photolithography.

To obtain g_{col}, we assume that the current within the loop is split equally and flows on the inner and outer edges of the superconducting loop. This is a more realistic flow compared with a single current loop or a uniform current density through the inductor cross section. We consider a cylindrical volume V with uniform doping density of 10^{17} cm^{-3} inside the inductor loop with a depth of 500 nm from the substrate surface. The x component of $\mathbf{B}_{ac}$ from both loops is then calculated at each individual spin location, giving a g_i for each spin i within V. Using an approach described in Ref. [44], we find that a histogram of g_i shows a relatively sharp peak at $g_{peak}/2\pi = 2.2$ kHz, and the number of spins within the full width at half maximum

is obtained as 4×10^5, yielding $g_{col}/2\pi = 1.4$ MHz. The value of g_{peak} is significantly smaller than the range of g shown in Fig. 3(b) for the single-atom device, primarily due to the larger inductor loop in the spin-ensemble device.

To simulate the device transmission spectrum when it is coupled to the spin ensemble, we consider the calculated value of g_{col} and use a theoretical model previously developed for a different quantum device with similar physics [45]. The model is based on the Jaynes-Cummings model [33] and the so-called input-output theory [46], with the assumption that the coupled spin ensemble can be treated as an oscillator in the limit of small power and low temperature [47]. The theory also treats the CPW as an extremely-low-Q ($Q_b \lesssim 1$) cavity with resonance frequency ω_b and photon annihilation operator $\hat{b}$. This allows accurate simulation of devices with asymmetric transmission [45]. The Hamiltonian now becomes $\mathcal{H} = \mathcal{H}_{JC} + \hbar\omega_b\hat{b}^\dagger\hat{b} + \hbar c(\hat{b}^\dagger\hat{a} + \hat{a}^\dagger\hat{b})$, where c is the coupling rate between the resonator and cavity b, and the spin-related parameters in $\mathcal{H}_{JC}$ are now associated with the spin *ensemble*. Figures 4(c) and 4(d) show the spectroscopy-simulation results obtained with $\tan\delta_0 = 10^{-4}$ and $Q_i = Q_e$ for the resonator with a symmetric transmission, and a conservative value of $T_1 = 100$ μs for the intrinsic (not Purcell-limited) relaxation time of the spin ensemble. In the presence of experimental spectroscopy data (not presented here), one can extract important parameters of this hybrid spin-resonator system directly with this theory. These parameters include g_{col}, the resonator Q, and the intrinsic relaxation time T_1 for the spin ensemble.
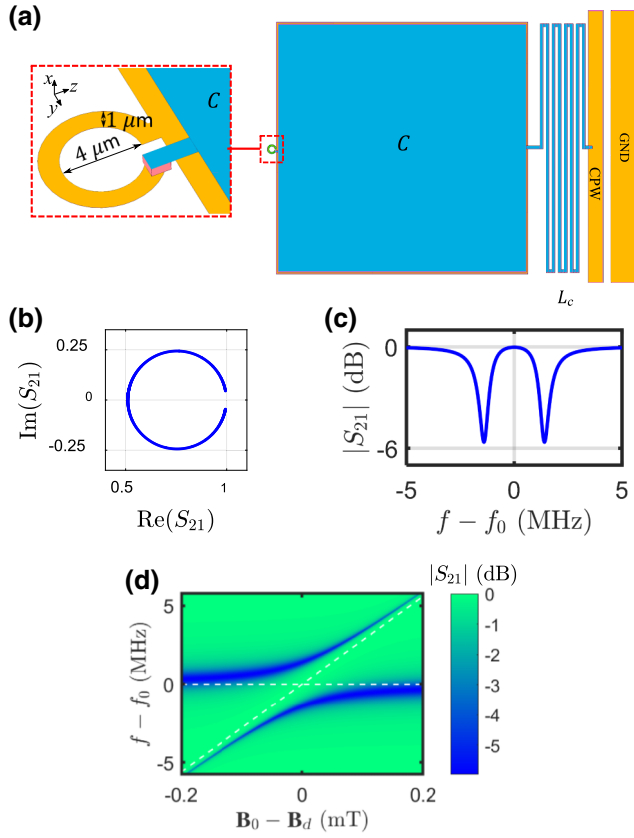
FIG. 4. (a) Layout of the simulated Al resonator coupled to an ensemble of Bi-donor electron spins (the ground plane surrounding the resonator and the Stark-shift electrodes are not shown). The dielectric thickness for the capacitor C is assumed to be $d = 50$ nm. (b) Simulated resonator transmission around its resonance frequency $f_0 = 7.2$ GHz in the absence of donors (no doping). Spectroscopy simulation of the hybrid resonator–spin-ensemble device near f_0 (c) for zero spin-resonator detuning and (d) with a tunable static magnetic field B_0 near the degeneracy field B_d.

From the high-frequency simulation, the geometric inductance of the loop is extracted as $L_{tot} = 8.5$ pH. Despite the significantly larger inductor dimensions of the spin-ensemble device, its impedance is similar to that of the single-atom device with a nanoscale spiral inductor for $N_{loops} = 2$–3, primarily due to the smaller contribution of the kinetic inductance in the spin-ensemble device. Therefore, we conclude that the CPW can also be sufficiently coupled to the single-atom device with the same (galvanic) coupling scheme.

IV. QUBIT OPERATION

The qubit operation parameters of the single-atom device presented in this paper are adopted from a commonly used cQED approach [15]. To estimate the initialization, manipulation, and readout performance, we focus on the Nb/P-2S configuration with $g/2\pi = 0.24$

MHz, $Q_i = 4 \times 10^4$, and $Q_e = 4 \times 10^5$, which are realizable according to our estimation of capacitive coupling [48] or galvanic coupling. We also assume that the bare-cavity resonance frequency is $\omega_0/2\pi = 5.6$ GHz and the Zeeman-splitting frequency ω_s is tunable around ω_0.

A. Initialization

The zero-detuning ($\Delta \equiv \omega_s - \omega_0 = 0$) relaxation time limited by the Purcell effect for this strongly coupled system is obtained as $T_{1,init} = \Gamma_P^{-1} = 2\kappa^{-1} = 2.3$ μs [49], which is several orders of magnitude smaller than the freespin relaxation time. The linear dependence of Γ_P on κ is a result of strong coupling, which distinguishes it from previously measured weakly coupled systems [36] where $\Gamma_P \propto g^2/\kappa$. Also, the 2-orders-of-magnitude increase in g in our device contributes to this dramatically fast initialization.

B. Manipulation

We can Stark shift the spin states using the electrodes shown in Fig. 2 or use a magnetic field to tune the Zeeman energy. For a demonstration of the qubit operation parameters of the device, we choose to operate at $\Delta = 40g$, where the strong-coupling Purcell rate is $\Gamma_P/2\pi = (1/4\pi)(\kappa - \sqrt{2}\sqrt{-A + \sqrt{A^2 + \kappa^2\Delta^2}}) = 88$ Hz, with $A \equiv \Delta^2 + 4g^2 - \kappa^2/4$ [49], giving rise to $T_{2,rot} = 2/\Gamma_P = 1.8$ ms. This relaxation time is not far from the measured Hahn-echo $T_2^H = 1.1$ ms for a P-donor electron spin in enriched ^{28}Si, which is believed to be limited primarily by the static-magnetic-field noise and thermal noise, and not by the proximity to the oxide layers or other amorphous material [9]. Therefore, it is reasonable to assume that the spin T_2 time in our device is Purcell limited, and hence is set by $T_{2,rot}$. For the Al/Bi set, the direction of the Stark shift must be such that the $|F, m_F\rangle = |5, -5\rangle \leftrightarrow |4, -4\rangle$ transition frequency, already reduced by a relatively small B_0 to lift the multiplet degeneracy, is further reduced to avoid exciting the higher-frequency multiplet transitions. In this dispersive regime ($\Delta \gg g$), the microwave drive frequency is $\omega_{\mu w}/2\pi = \omega_s/2\pi + (2n_{lim} + 1)g^2/2\pi\Delta = 5.614406$ GHz, where photon number $n_{lim} = \Delta^2/4g^2 = 400$ sets the maximum limit for the drive power [15] and is lower than the critical photon number $n_{crit} \approx 1800$ corresponding to the spiral inductor's critical current. The qubit rotation speed, at on-resonance photon number $n_{res} \approx 17 \times 10^6$ set by n_{lim} and $\omega_{\mu w}$, is $f_{rot} = g\kappa\sqrt{n_{res}}/\pi\Delta = 29$ MHz [50], corresponding to $N_\pi = 2f_{rot}T_{2,rot} > 10^5$ coherent π rotations.

C. Readout

The spin readout also occurs in the dispersive regime, where the cavity frequency depends on the spin state, giving rise to separation frequency $f_{sep} =$

$g^2/\pi\Delta = 12$ kHz. This corresponds to a phase shift of $\phi = 2\arctan(2g^2/\kappa\Delta) = 10°$, well above the measurement sensitivity usually considered to be $0.1°$, and suggests an extremely high-fidelity readout when the resonator is driven at ω_0. The measurement time to resolve ϕ is estimated to be $T_m = (2\kappa n_{\text{read}}\theta_0^2)^{-1} = 3.1$ μs, where $\theta_0 \equiv 2g^2/\kappa\Delta$ [15] and $n_{\text{read}} = 25$ is the readout photon number. To avoid the highly-nonlinear-response regime, the readout power must be limited to $n_{\text{read}} \lesssim \Delta^2/4g^2$.

V. CONCLUSION

In summary, we propose and design a device that enhances the coupling of a single-atom electron spin to the magnetic field of a circuit resonator by approximately 100 times compared with the previously proposed architectures that use coplanar resonators. This dramatic increase is a result of the use of a low-impedance, lumped-element resonator design and a nanoscale spiral inductor geometry. We show the possibility of entering the strong-coupling regime necessary for practical purposes (i.e., spectroscopic measurements and qubit realization). Using the well-established principles of cavity quantum electrodynamics, we show that this large g can lead to a significantly enhanced spin relaxation rate, which is desired for qubit initialization, tens-of-megahertz spin rotation speed during manipulation without the need for an Oersted line, and superb dispersive readout sensitivity. Moreover, this architecture can be useful for coupling distant qubits using cavity photons for the realization of multiqubit gates. We emphasize that this large enhancement in the coupling rate results directly from increasing the ac magnetic field at the spin, rather than by hybridizing the spin and charge states through, for example, a magnetic field gradient generated by local micromagnets. In this way, we believe that a relatively large spin-photon coupling rate can be achieved while avoiding a concomitant increase in the charge-noise-induced decoherence rate [24,25].

We also propose a relatively simple proof-of-principle experiment that does not require single-donor implantation or electron-beam lithography. This simplified scheme takes advantage of the resonator's enhanced coupling to a spin ensemble, which is expected to result in the direct observation of the vacuum Rabi splitting to confirm strong coupling.

APPENDIX: INDUCTANCE SIMULATIONS, MAGNETIC FIELD, AND COUPLING-RATE CALCULATION

The total inductance $L_{\text{tot}} = L_g + L_p$ within the resonator consists of the geometric inductance L_g of the spiral inductor giving rise to the magnetic field $\mathbf{B}_{\text{ac}}$ that couples to the donor electron spin, and parasitic inductance L_p that does not contribute to $\mathbf{B}_{\text{ac}}$ and only limits it. L_g consists of the trace inductance L_t arising from the length of the spiral trace, and some mutual inductance L_M between the loops such that $L_g = L_t + L_M$. The parasitic inductance L_p includes the kinetic inductance L_k of the spiral, the kinetic inductance $L_{C,k}$ within the capacitor plates, and the geometric self-inductance $L_{C,g}$ of the capacitor such that $L_p = L_k + L_{C,k} + L_{C,g}$. Since L_p does not create magnetic fields at the location of the spin and only limits I_{ac} through L_{tot}, we want to minimize it. To obtain an accurate estimation of L_g and L_p, we perform calculations as well as software simulations. We study two device geometries, one with a single-layer spiral inductor and the other with a 2S inductor, shown in Figs. 1(c) and 2, respectively.

L_g is approximately calculated, and also separately simulated. In the calculations, for simplicity, we assume that each loop of the spiral inductor is perfectly circular and estimate L_g using the geometric-mean-distance method to the second order in the ratio of the conductor diameter to the loop radius [51]. This independent-loop approximation ignores the mutual inductance L_M within the spiral loops. However, one should note that L_M contributes to $\mathbf{B}_{\text{ac}}$ and is not parasitic. Nevertheless, in addition to the independent-loop approximation, we also simulate the spiral geometry in the FastHenry three-dimensional inductance extraction program [52], which accounts for the mutual inductances L_M within the spiral geometry. Figure 5 shows a comparison between the simulation and the approximate calculation, where the latter ignores L_M. Clearly, L_M constitutes a larger portion of L_g with increasing N_{loops}, but is negligible up to $N_{\text{loops}} = 2$, where g is optimum [see Fig. 3(b)]. The total inductance L_{tot} in Fig. 3(a) is plotted with L_g from FastHenry simulations. However, for simplicity, the ac field contributed by L_M is not taken into account in our calculating g, resulting in an underestimated g in Fig. 3(b).

The kinetic inductance L_k of the spiral loop is caused by the kinetic energy of the quasiparticles within the superconductor and hence does not create any magnetic fields. In our design, L_k is the largest part of L_p. Using the Cooper-pair density n_s and mass m_C for a superconducting material and the length of the superconducting line l_s and its cross-section area A_s, one can estimate $L_k = m_C l_s/4n_s e^2 A_s$
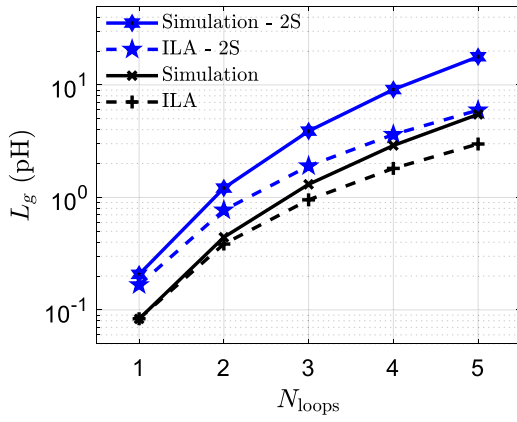
FIG. 5. Comparison between the independent-loop approximation (ILA) and FastHenry simulations of the spiral's geometric inductance versus spiral loop counts N_{loops} for the single-spiral and 2S geometries.

[53], where e denotes the electron charge. For the single-layer spiral Nb/P resonator with $1 \leq N_{loops} \leq 5$, we obtain $0.6 \text{ pH} \leq L_k \leq 7 \text{ pH}$, which is linearly proportional to the spiral trace length.

The kinetic inductance within the capacitor plates, $L_{C,k} \approx 60$ fH, is negligible due to the large cross-section area of the plates. The geometric self-inductance of the capacitor, calculated with a stripline model, is $L_{C,g} \approx 62$ fH, and is suppressed by use of a relatively thin capacitor insulating layer (small d_0). To confirm this, we simulate the resonator geometry including the capacitor and find $L_{C,g} = 64$ fH, in agreement with the calculated value and also negligible for $N_{loops} = 2$.

To achieve the desired resonance frequencies with the relatively small inductances shown in Fig. 3(a), relatively large capacitances are required. By using a capacitor insulator thickness of $d_0 = 25$ nm in the single-atom device, we can keep the square-shaped capacitor dimensions below 200 μm, while significantly suppressing $L_{C,g}$.

For the single-atom device, a simulation of g as a function of the spiral trace width w, spacing s, and thickness t is performed. By our assuming $w = s = t$, the results show that, for the Nb (Al) set, the optimum g is obtained when $30 \text{ nm} \lesssim w = s = t \lesssim 35 \text{ nm}$ ($w = s = t \approx 20$ nm), weakly depending on whether the single-layer spiral geometry or the 2S geometry is used. If electron-beam-lithography resolution of 20 nm is implemented, the Al set can yield a spin-photon coupling rate of $g/2\pi = 0.45$ MHz for $N_{loops} = 2$.

At the location of the spin in the single-atom device, B_{ac} is approximated as the sum of the magnetic field from all loops; that is, $B_{ac} = \sum_{loops} \mu_0 I_{ac}/2R'_{loop}$, where $R'_{loop} \equiv (d_{in}^2 + 4d_s^2)^{3/2}/2d_{in}^2$ is a characteristic radius that accounts for the spin location with respect to the center of the loops and d_s denotes the vertical spin displacement

from this center [see Figs. 1(c) and 4]. The assumption that the current flows in the center of the spiral superconductor underestimates B_{ac}, $B_{ac,0}$, and g, because in reality most of the current will flow closer to the superconductor-silicon interface due to the relatively large electric permittivity ($\epsilon_r = 12$) of silicon.

For better understanding of the dependence of g on the number N_{loops} of spiral loops, a naive picture may be helpful to the reader. To the first order for $N_{loops} = 1$, we have $I_{ac} \propto 1/\sqrt{L_g + L_p}$, $L_g \propto N_{loops}^2 \ln(N_{loops})$, and $B_{ac,0}, g \propto I_{ac} \ln(N_{loops})$, but L_p is a weaker function of N_{loops} than L_g. This suggest that by increase of N_{loops}, $B_{ac,0}$ and hence g increase up to a point where L_g approaches L_p, and I_{ac} begins to drop as N^α, with $\alpha < -1$. Use of a lumped-element design provides the required flexibility to reach this optimum L_g and the corresponding N_{loops}.

[1] R. Hanson, L. P. Kouwenhoven, J. R. Petta, S. Tarucha, and L. M. K. Vandersypen, Spins in few-electron quantum dots, Rev. Mod. Phys. **79**, 1217 (2007).

[2] Daniel Loss and David P. DiVincenzo, Quantum computation with quantum dots, Phys. Rev. A **57**, 120 (1998).

[3] Jason R. Petta, Alexander Comstock Johnson, Jacob M. Taylor, Edward A. Laird, Amir Yacoby, Mikhail D. Lukin, Charles M. Marcus, Micah P. Hanson, and Arthur C. Gossard, Coherent manipulation of coupled electron spins in semiconductor quantum dots, Science **309**, 2180 (2005).

[4] Floris A. Zwanenburg, Andrew S. Dzurak, Andrea Morello, Michelle Y. Simmons, Lloyd C. L. Hollenberg, Gerhard Klimeck, Sven Rogge, Susan N. Coppersmith, and Mark A. Eriksson, Silicon quantum electronics, Rev. Mod. Phys. **85**, 961 (2013).

[5] Jarryd J. Pla, Kuan Y. Tan, Juan P. Dehollain, Wee H. Lim, John J. L. Morton, David N. Jamieson, Andrew S. Dzurak, and Andrea Morello, A single-atom electron spin qubit in silicon, Nature **489**, 541 (2012).

[6] Kamyar Saeedi, Stephanie Simmons, Jeff Z. Salvail, Phillip Dluhy, Helge Riemann, Nikolai V. Abrosimov, Peter Becker, Hans-Joachim Pohl, John J. L. Morton, and Mike L. W. Thewalt, Room-temperature quantum bit storage exceeding 39 minutes using ionized donors in silicon-28, Science **342**, 830 (2013).

[7] Alexei M. Tyryshkin, Shinichi Tojo, John J. L. Morton, Helge Riemann, Nikolai V. Abrosimov, Peter Becker, Hans-Joachim Pohl, Thomas Schenkel, Michael L. W. Thewalt, Kohei M. Itoh, and S. A. Lyon, Electron spin coherence exceeding seconds in high-purity silicon, Nat. Mater. **11**, 143 (2012).

[8] M. Steger, K. Saeedi, M. L. W. Thewalt, J. J. L. Morton, H. Riemann, N. V. Abrosimov, P. Becker, and H.-J. Pohl, Quantum information storage for over 180 s using donor spins in a 28Si semiconductor vacuum, Science **336**, 1280 (2012).

[9] Juha T. Muhonen, Juan P. Dehollain, Arne Laucht, Fay E. Hudson, Rachpon Kalra, Takeharu Sekiguchi, Kohei M. Itoh, David N. Jamieson, Jeffrey C. McCallum, Andrew S. Dzurak, and Andrea Morello, Storing quantum information

for 30 seconds in a nanoelectronic device, Nat. Nanotech. **9**, 986 (2014).

[10] David D. Awschalom, Lee C. Bassett, Andrew S. Dzurak, Evelyn L. Hu, and Jason R. Petta, Quantum spin-tronics: Engineering and manipulating atom-like spins in semiconductors, Science **339**, 1174 (2013).

[11] Andreas Wallraff, David I. Schuster, Alexandre Blais, L. Frunzio, R.-S. Huang, J. Majer, S. Kumar, Steven M. Girvin, and Robert J. Schoelkopf, Strong coupling of a single photon to a superconducting qubit using circuit quantum electrodynamics, Nature **431**, 162 (2004).

[12] Xiu Gu, Anton Frisk Kockum, Adam Miranowicz, Yu-xi Liu, and Franco Nori, Microwave photonics with superconducting quantum circuits, Phys. Rep. **718-719**, 1 (2017).

[13] J. Majer, J. M. Chow, J. M. Gambetta, Jens Koch, B. R. Johnson, J. A. Schreier, L. Frunzio, D. I. Schuster, A. A. Houck, Andreas Wallraff, *et al.*, Coupling superconducting qubits via a cavity bus, Nature **449**, 443 (2007).

[14] B. Sarabi, A. N. Ramanayaka, A. L. Burin, F. C. Wellstood, and K. D. Osborn, Projected Dipole Moments of Individual Two-level Defects Extracted using Circuit Quantum Electrodynamics, Phys. Rev. Lett. **116**, 167002 (2016).

[15] Alexandre Blais, Ren-Shou Huang, Andreas Wallraff, S. M. Girvin, and R. J. Schoelkopf, Cavity quantum electrodynamics for superconducting electrical circuits: An architecture for quantum computation, Phys. Rev. A **69**, 062320 (2004).

[16] C. Eichler, A. J. Sigillito, S. A. Lyon, and J. R. Petta, Electron Spin Resonance at the Level of 10^4 Spins using Low Impedance Superconducting Resonators, Phys. Rev. Lett. **118**, 037701 (2017).

[17] Atac Imamoğlu, Cavity QED based on Collective Magnetic Dipole Coupling: Spin Ensembles as Hybrid Two-level Systems, Phys. Rev. Lett. **102**, 083602 (2009).

[18] Guilherme Tosi, Fahd A. Mohiyaddin, Hans Huebl, and Andrea Morello, Circuit-quantum electrodynamics with direct magnetic coupling to single-atom spin qubits in isotopically enriched ^{28}Si, AIP Adv. **4**, 087122 (2014).

[19] Y. Kubo, F. R. Ong, P. Bertet, D. Vion, V. Jacques, D. Zheng, A. Dréau, J.-F. Roch, A. Auffeves, F. Jelezko, J. Wrachtrup, M. F. Barthe, P. Bergonzo, and D. Esteve, Strong Coupling of a Spin Ensemble to a Superconducting Resonator, Phys. Rev. Lett. **105**, 140502 (2010).

[20] R. Amsüss, Ch. Koller, T. Nöbauer, S. Putz, S. Rotter, K. Sandner, S. Schneider, M. Schramböck, G. Steinhauser, H. Ritsch, J. Schmiedmayer, and J. Majer, Cavity QED with Magnetically Coupled Collective Spin States, Phys. Rev. Lett. **107**, 060502 (2011).

[21] K. D. Petersson, L. W. McFaul, M. D. Schroer, M. Jung, J. M. Taylor, A. A. Houck, and J. R. Petta, Circuit quantum electrodynamics with a spin qubit, Nature **490**, 380 (2012).

[22] J. J. Viennot, M. C. Dartiailh, A. Cottet, and T. Kontos, Coherent coupling of a single spin to microwave cavity photons, Science **349**, 408 (2015).

[23] Xuedong Hu, Yu-xi Liu, and Franco Nori, Strong coupling of a spin qubit to a superconducting stripline cavity, Phys. Rev. B **86**, 035314 (2012).

[24] Xiao Mi, Mónica Benito, Stefan Putz, David M. Zajac, Jacob M. Taylor, Guido Burkard, and Jason R. Petta, A

[25] N. Samkharadze, G. Zheng, N. Kalhor, D. Brousse, A. Sammak, U. C. Mendes, A. Blais, G. Scappucci, and L. M. K. Vandersypen, Strong spin-photon coupling in silicon, Science **359**, 1123 (2018).

coherent spin–photon interface in silicon, Nature **555**, 599 (2018).

[26] Y. Kubo, C. Grezes, A. Dewes, T. Umeda, J. Isoya, H. Sumiya, N. Morishita, H. Abe, S. Onoda, T. Ohshima, V. Jacques, A. Dréau, J.-F. Roch, I. Diniz, A. Auffeves, D. Vion, D. Esteve, and P. Bertet, Hybrid Quantum Circuit with a Superconducting Qubit Coupled to a Spin Ensemble, Phys. Rev. Lett. **107**, 220501 (2011).

[27] J. Twamley and S. D. Barrett, Superconducting cavity bus for single nitrogen-vacancy defect centers in diamond, Phys. Rev. B **81**, 241202 (2010).

[28] R. W. Simmonds, K. M. Lang, D. A. Hite, S. Nam, D. P. Pappas, and John M. Martinis, Decoherence in Josephson Phase Qubits from Junction Resonators, Phys. Rev. Lett. **93**, 077003 (2004).

[29] John M. Martinis, K. B. Cooper, R. McDermott, Matthias Steffen, Markus Ansmann, K. D. Osborn, K. Cicak, Seongshik Oh, D. P. Pappas, R. W. Simmonds, and Clare C. Yu, Decoherence in Josephson Qubits from Dielectric Loss, Phys. Rev. Lett. **95**, 210503 (2005).

[30] P. Kumar, S. Sendelbach, M. A. Beck, J. W. Freeland, Zhe Wang, Hui Wang, Clare C. Yu, R. Q. Wu, D. P. Pappas, and R. McDermott, Origin and Reduction of $1/f$ Magnetic Flux Noise in Superconducting Devices, Phys. Rev. Appl. **6**, 041001 (2016).

[31] Arne Laucht, Juha T. Muhonen, Fahd A. Mohiyaddin, Rachpon Kalra, Juan P. Dehollain, Solomon Freer, Fay E. Hudson, Menno Veldhorst, Rajib Rahman, Gerhard Klimeck, Kohei M. Itoh, David N. Jamieson, Jeffrey C. McCallum, Andrew S. Dzurak, and Andrea Morello, Electrically controlling single-spin qubits in a continuous microwave field, Sci. Adv. **1**, e1500022 (2015).

[32] Yasuhiro Tokura, Wilfred G. van der Wiel, Toshiaki Obata, and Seigo Tarucha, Coherent Single Electron Spin Control in a Slanting Zeeman Field, Phys. Rev. Lett. **96**, 047202 (2006).

[33] E. T. Jaynes and F. W. Cummings, Comparison of quantum and semiclassical radiation theories with application to the beam maser, P. IEEE **51**, 89 (1963).

[34] Michael R. Vissers, Johannes Hubmayr, Martin Sandberg, Saptarshi Chaudhuri, Clint Bockstiegel, and Jiansong Gao, Frequency-tunable superconducting resonators via nonlinear kinetic inductance, Appl. Phys. Lett. **107**, 062601 (2015).

[35] Gary Wolfowicz, Stephanie Simmons, Alexei M. Tyryshkin, Richard E. George, Helge Riemann, Nikolai V. Abrosimov, Peter Becker, Hans-Joachim Pohl, Stephen A. Lyon, Mike L. W. Thewalt, and John J. L. Morton, Decoherence mechanisms of ^{209}Bi donor electron spins in isotopically pure ^{28}Si, Phys. Rev. B **86**, 245301 (2012).

[36] A. Bienfait, J. J. Pla, Y. Kubo, X. Zhou, M. Stern, C. C. Lo, C. D. Weis, T. Schenkel, D. Vion, D. Esteve, J. J. L. Morton, and P. Bertet, Controlling spin relaxation with a cavity, Nature **531**, 74 (2016).

[37] M. H. Mohammady, G. W. Morley, and T. S. Monteiro, Bismuth Qubits in Silicon: The Role of EPR Cancellation Resonances, Phys. Rev. Lett. **105**, 067602 (2010).

[38] Martin Fuechsle, Jill A. Miwa, Suddhasatta Mahapatra, Hoon Ryu, Sunhee Lee, Oliver Warschkow, Lloyd C. L. Hollenberg, Gerhard Klimeck, and Michelle Y. Simmons, A single-atom transistor, Nat. Nanotech. **7,** 242 (2012).

[39] J. Romijn, T. M. Klapwijk, M. J. Renne, and J. E. Mooij, Critical pair-breaking current in superconducting aluminum strips far below T_c, Phys. Rev. B **26,** 3648 (1982).

[40] R. Huebener, R. Kampwirth, R. Martin, T. Barbee, and R. Zubeck, Critical current density in superconducting niobium films, IEEE T. Magn. **11,** 344 (1975).

[41] Aaron D. O'Connell, M. Ansmann, R. C. Bialczak, M. Hofheinz, N. Katz, Erik Lucero, C. McKenney, M. Neeley, H. Wang, E. M. Weig, A. N. Cleland, and J. M. Martinis, Microwave dielectric loss at single photon energies and millikelvin temperatures, Appl. Phys. Lett. **92,** 112903 (2008).

[42] Xiao Liu, Daniel R. Queen, Thomas H. Metcalf, Julie E. Karel, and Frances Hellman, Hydrogen-free Amorphous Silicon with No Tunneling States, Phys. Rev. Lett. **113,** 025503 (2014).

[43] C. Jagannath, Z. W. Grabowski, and A. K. Ramdas, Linewidths of the electronic excitation spectra of donors in silicon, Phys. Rev. B **23,** 2082 (1981).

[44] A. Bienfait, J. J. Pla, Y. Kubo, M. Stern, X. Zhou, C. C. Lo, C. D. Weis, T. Schenkel, M. L. W. Thewalt, D. Vion, D. Esteve, B. Julsgaard, K. Mølmer, J. J. L. Morton, and P. Bertet, Reaching the quantum limit of sensitivity in electron spin resonance, Nat. Nanotech. **11,** 253 (2016).

[45] Bahman Sarabi, Ph.D. thesis, school University of Maryland, College Park, 2014.

[46] M. J. Collett and C. W. Gardiner, Squeezing of intracavity and traveling-wave light fields produced in parametric amplification, Phys. Rev. A **30,** 1386 (1984).

[47] B. Sarabi, A. N. Ramanayaka, A. L. Burin, F. C. Wellstood, and K. D. Osborn, Cavity quantum electrodynamics using a near-resonance two-level system: Emergence of the Glauber state, Appl. Phys. Lett. **106,** 172601 (2015).

[48] John M. Martinis, Rami Barends, and Alexander N. Korotkov, Calculation of coupling capacitance in planar electrodes, arXiv:1410.3458.

[49] Eyob A. Sete, Jay M. Gambetta, and Alexander N. Korotkov, Purcell effect with microwave drive: Suppression of qubit relaxation rate, Phys. Rev. B **89,** 104516 (2014).

[50] S. Haroche, in *Fundamental Systems in Quantum Optics*, edited by J. Dalibard, J. M. Raimond, and J. Zinn-Justin (Elsevier Science Publishers B.V., Amsterdam, 1993) Chap. Cavity Quantum Electrodynamics, p. 767.

[51] Frederick W. Grover, *Inductance Calculations: Working Formulas and Tables* (Dover, New York, 1962).

[52] Mattan Kamon, Michael J. Tsuk, and Jacob K. White, Fasthenry: A multipole-accelerated 3-D inductance extraction program, IEEE Trans. Microw. Theory Tech. **42,** 1750 (1994).

[53] Michael Tinkham, *Introduction to Superconductivity* (McGraw-Hill, New York, 1996).